Spatial dynamics of laser-induced fluorescence in an intense laser beam: An experimental and theoretical study with alkali-metal atoms

M. Auzinsh,* A. Berzins, R. Ferber, F. Gahbauer, and U. Kalnins
Laser Centre, The University of Latvia, 19 Rainis Boulevard, LV-1586 Riga, Latvia
(Received 27 October 2015; revised manuscript received 27 January 2016; published 3 March 2016)

We show that it is possible to model accurately optical phenomena in intense laser fields by taking into account the intensity distribution over the laser beam. We present an extension of an earlier theoretical model that divides an intense laser beam into concentric regions, each with a Rabi frequency that corresponds to the intensity in that region, and solve a set of coupled optical Bloch equations for the density matrix in each region. Experimentally obtained magneto-optical resonance curves for the $F_g = 2 \longrightarrow F_e = 1$ transition of the D_1 line of ^{87}Rb agree very well with the theoretical model up to a laser intensity of around 200 mW/cm^2 for a transition whose saturation intensity is around 4.5 mW/cm^2. We examine the spatial dependence of the fluorescence intensity in an intense laser beam experimentally and theoretically. We present and discuss the results of an experiment in which a broad, intense pump laser excites the $F_g = 4 \longrightarrow F_e = 4$ transition of the D_2 line of cesium while a narrow probe beam scans the atoms within the pump beam and excites the D_1 line of cesium, whose fluorescence is recorded as a function of probe beam position. Experimentally obtained spatial profiles of the fluorescence intensity agree qualitatively with the predictions of the model.

DOI: 10.1103/PhysRevA.93.033403

I. INTRODUCTION

Coherent radiation can polarize the angular momentum distribution of an ensemble of atoms in various ways, creating different polarization moments, which modify the way these atoms will interact with radiation. Carefully prepared spin polarized atoms can make the absorption highly dependent on frequency (electromagnetically induced transparency [1]), causing large values of the dispersion, which, in turn, are useful for such interesting effects as slow light [2] and optical information storage [3]. Electric and magnetic fields, external or inherent in the radiation fields, may also influence the time evolution of the spin polarization and cause measurable changes in absorption or fluorescence intensity and/or polarization. These effects are the basis of many magnetometry schemes [4,5], and must be taken into account in atomic clocks [6] and when searching for fundamental symmetry violations [7] or exotic physics such as an electric dipole moment of the electron [8]. Sufficiently strong laser radiation creates atomic coherences in the excited as well as in the ground state [9]. The coherences are destroyed when the Zeeman sublevel degeneracy is removed by a magnetic field. Since the ground state has a much longer lifetime, very narrow magneto-optical resonances can be created, which are related to the ground-state Hanle effect (see [10] for a review). Such resonances were first observed in cadmium in 1964 [11].

The formation of dark magneto-optical resonances has been understood for some time (see [7,9,12] for a review), and bright (opposite sign) magneto-optical resonances have also been observed and explained [13–15]; the challenge in describing experiments lies in choosing the effects to be included in the numerical calculations so as to find a balance between computation time and accuracy. The optical Bloch equations (OBEs) for the density matrix have been used as early as 1978 to model magneto-optical resonances [16]. In order to achieve greater accuracy, later efforts to model signals took into account effects such as Doppler broadening, the coherent properties of the laser radiation, and the mixing of magnetic sublevels in an external magnetic field to produce more and more accurate descriptions of experimental signals [17]. Analytical models can also achieve excellent descriptions of experimental signals under weak excitation, i.e., in the lowest nonlinear order of laser power [18,19]. In recent years, excellent agreement has been achieved by numerical calculations even when optical pumping plays a role. However, as soon as the laser radiation begins to saturate the absorption transition, the model's accuracy suffers. The explanation has been that at high radiation intensities, it is no longer possible to model the relaxation of atoms moving in and out of the beam with a single rate constant [17,20]. Nevertheless, accurate numerical models of magneto-optical effects in an intense laser field are very desirable, because they could arise in a number of experimental situations [18,19,21–24]. Therefore, we have set out to model magneto-optical effects in the presence of intense laser radiation by taking into account the fact that an atom experiences different laser intensity values as it passes through a beam. In practice, we solve the rate equations for the Zeeman coherences for different regions of the laser beam with a value of the Rabi frequency that more closely approximates the real situation in that part of the beam. To save computing time, stationary solutions to the rate equations for Zeeman sublevels and coherences are sought for each region [25]. With this simplification, and by taking into account the motion of atoms through the beam, we can now obtain accurate descriptions of experimental signals up to much higher intensities while maintaining reasonable computing times. Moreover, the model can be used to study the spatial distribution of the laser induced fluorescence within the laser beam. We report here the results of a theoretical and experimental study that involves two overlapping lasers: one spatially broad, intense pump laser, and a weaker, tightly focused, spatially narrow probe laser. The qualitative agreement between experimental and theoretical fluorescence intensity profiles indicates that the model is a

*Marcis.Auzins@lu.lv

useful tool for studying fluorescence dynamics as well as for modeling magneto-optical signals at high laser intensities.

II. THEORY

The theoretical model used here is a further development of previous efforts [26], which has been subjected to some initial testing in the specialized context of an extremely thin cell [24]. The description of coherent processes starts with the OBE:

$$i\hbar\frac{\partial\rho}{\partial t} = [\hat{H},\rho] + i\hbar\hat{R}\rho, \tag{1}$$

where ρ is the density matrix describing the atomic state, $\hat{H}$ is the Hamiltonian of the system, and $\hat{R}$ is an operator that describes relaxation. These equations are transformed into rate equations that are solved under stationary conditions in order to obtain the Zeeman coherences in the ground ($\rho_{g_i g_j}$) and excited ($\rho_{e_i e_j}$) states [25]. However, when the intensity distribution in the beam is not homogeneous, more accurate results can be achieved by dividing the laser beam into concentric regions and solving the OBEs for each region separately, while accounting for atoms that move into and out of each region as they fly through the beam. Figure 1 illustrates the idea.

The top part of the figure shows the intensity profile of the laser beam, while the bottom part of the figure shows a cross section of the laser beam indicating the concentric regions.

In order to account for particles that leave one region and enter the next, an extra term must be added to the OBE:

$$-i\hbar\hat{\gamma}_t\rho + i\hbar\hat{\gamma}_t\rho'. \tag{2}$$

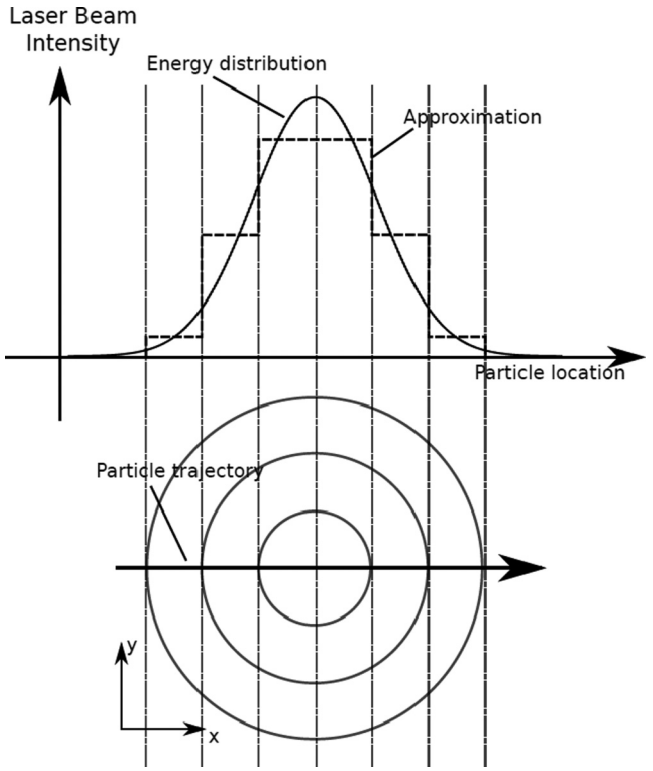

FIG. 1. Laser beam profile split into a number of concentric regions.

In this term, ρ' is the density matrix of the particles entering the region with index $n+1$ (identical to the density matrix of the particles leaving the previous region), and $\hat{\gamma}_t$ is an operator that accounts for transit relaxation. This operator is essentially a diagonal matrix with elements $\hat{\gamma}_{t_{ij}} = (v_{yz}s_n)\delta_{ij}$, where v_{yz} characterizes the particle speed in the plane perpendicular to the beam and s_n is the linear dimension of the region. To simplify matters, we treat particle motion in only one direction and later average with particles that move in the other direction. In that case, $\rho' = \rho^{n-1}$. Thus, the rate equations for the density matrix ρ^n of the n^{th} region become

$$\begin{aligned} i\hbar\frac{\partial\rho^n}{\partial t} &= [\hat{H},\rho^n] + i\hbar\hat{R}\rho^n - i\hbar\hat{\gamma}_t{}^n\rho^n \\ &\quad + i\hbar\hat{\gamma}_t{}^n\rho^{n-1} - i\hbar\hat{\gamma}_c\rho^n + i\hbar\hat{\gamma}_c\rho^0. \end{aligned} \tag{3}$$

In this equation the relaxation operator $\hat{R}$ describes spontaneous relaxation only and $\hat{\gamma}_c$ is the collisional relaxation rate, which, however, becomes significant only at higher gas densities.

Next, the rotating wave approximation [27] is applied to the OBEs, which yield stochastic differential equations that can be simplified by means of the decorrelation approach [28]. Since the measurable quantity is merely light intensity, a formal statistical average is performed over the fluctuating phases of these stochastic equations, making use of the decorrelation approximation [25]. As a result, the density matrix elements that correspond to optical coherences are eliminated and one is left with rate equations for the Zeeman coherences:

$$\begin{aligned} \frac{\partial\rho^n_{g_i,g_j}}{\partial t} &= \sum_{e_k,e_m}\left(\Xi^n_{g_i e_m} + \left(\Xi^n_{e_k g_j}\right)^*\right)d^*_{g_i e_k}d_{e_m g_j}\rho^n_{e_k e_m} \\ &\quad - \sum_{e_k,g_m}\left(\Xi^n_{e_k g_j}\right)^* d^*_{g_i e_k}d_{e_k g_m}\rho^n_{g_m g_j} \\ &\quad - \sum_{e_k,g_m}\Xi^n_{g_i e_k}d^*_{g_m e_k}d_{e_k g_j}\rho^n_{g_i g_m} \\ &\quad - i\omega_{g_i g_j}\rho^n_{g_i g_j} + \sum_{e_k e_l}\Gamma^{e_k e_l}_{g_i g_j}\rho^n_{e_k e_l} - \gamma_t\rho^n_{g_i g_j} \\ &\quad + \gamma^n_t\rho^{n-1}_{g_i g_j} - \gamma^n_c\rho^n_{g_i g_j} + \gamma_c\rho^0_{g_i g_j}. \end{aligned} \tag{4}$$

$$\begin{aligned} \frac{\partial\rho^n_{e_i,e_j}}{\partial t} &= \sum_{g_k,g_m}\left(\left(\Xi^n_{e_i g_m}\right)^* + \Xi^n_{g_k e_j}\right)d^*_{e_i g_k}d_{g_m e_j}\rho^n_{g_k g_m} \\ &\quad - \sum_{g_k,e_m}\Xi^n_{g_k e_j}d_{e_i g_k}d^*_{g_k e_m}\rho^n_{e_m e_j} \\ &\quad - \sum_{g_k,e_m}\left(\Xi^n_{e_i g_k}\right)^* d_{e_m g_k}d^*_{g_k e_j}\rho^n_{e_i e_m} \\ &\quad - i\omega_{e_i e_j}\rho^n_{e_i e_j} - \Gamma\rho^n_{e_i e_j} - \gamma^n_t\rho^n_{e_i e_j} \\ &\quad + \gamma^n_t\rho^{n-1}_{e_i e_j} - \gamma_c\rho^n_{e_i e_j}. \end{aligned} \tag{5}$$

In both equations, the first term describes the population increase and the creation of coherence as a result of induced transitions, the second and third terms describe population loss due to induced transitions, and the fourth term describes the destruction of Zeeman coherences due to the respective splitting $\omega_{g_i g_j}$ or $\omega_{e_i e_j}$ of the Zeeman sublevels in an external

magnetic field. The fifth term in Eq. (5) describes spontaneous decay with $\Gamma\rho^n_{e_ie_j}$ giving the spontaneous rate of decay for the excited state. At the same time the fifth term in Eq. (4) describes the transfer of population and coherences from the excited-state matrix element $\rho_{e_ke_l}$ to the ground-state density matrix element $\rho_{g_ig_j}$ with rate $\Gamma^{e_ke_l}_{g_ig_j}$. These transfer rates are related to the rate of spontaneous decay Γ for the excited state. Explicit expressions for these $\Gamma^{e_ke_i}_{g_ig_j}$ can be calculated from quantum angular momentum theory and are given in [9]. The remaining terms have been described previously in the context of Eqs. (2) and (3). The laser beam interaction is represented by an interaction term,

$$\Xi_{g_ie_j} = \frac{|\boldsymbol{\varepsilon}^n|^2}{\frac{\Gamma+\Delta\omega}{2} + i\left(\bar{\omega} - \mathbf{k}\cdot\mathbf{v} + \omega_{g_ie_j}\right)}, \tag{6}$$

where $|\boldsymbol{\varepsilon}^n|^2$ is the laser field's electric field strength in the nth region, Γ is the spontaneous decay rate, $\Delta\omega$ is the laser beam's spectral width, $\bar{\omega}$ is the laser frequency, $k\cdot v$ gives the Doppler shift, and $\omega_{g_ie_j}$ is the difference in energy between levels g_i and e_j. The system of linear equations can be solved for stationary conditions to obtain the density matrix ρ.

From the density matrix one can obtain the fluorescence intensity from each region for each velocity group v and given polarization $\boldsymbol{\varepsilon}_f$ up to a constant factor of $\tilde{I}_0$ [29–31]:

$$I_n(v,\boldsymbol{\varepsilon}_f) = \tilde{I}_0 \sum_{g_i,e_j,e_k} d^{*(ob)}_{g_ie_j} d^{(ob)}_{e_kg_i} \rho_{e_je_k}. \tag{7}$$

From these quantities one can calculate the total fluorescence intensity for a given polarization $\boldsymbol{\varepsilon}_f$:

$$I(\boldsymbol{\varepsilon}_f) = \sum_n \sum_v f(v)\Delta v \frac{A_n}{A} I_n(v,\boldsymbol{\varepsilon}_f). \tag{8}$$

Here the sum over n represents the sum over the different beam regions of relative area A_nA as they are traversed by the particle, v is the particle velocity along the laser beam, and $f(v)\Delta v$ gives the number of atoms with velocity $v \pm \Delta v2$.

In practice, we do not measure the electric field strength of the laser field, but the intensity $I = P/A$, where P is the laser power and A is the cross-sectional area of the beam. In the theoretical model it is more convenient to use the Rabi frequency Ω_R, here defined as follows:

$$\Omega_R = k_R \frac{\|d\|\cdot\|\epsilon\|}{\hbar} = k_R \frac{\|d\|}{\hbar}\sqrt{\frac{2I}{\epsilon_0 nc}}, \tag{9}$$

where $||d||$ is the reduced dipole matrix element for the transition in question, ϵ_0 is the vacuum permittivity, n is the index of refraction of the medium, c is the speed of light, and k_R is a factor that would be unity in an ideal case, but is adjusted to achieve the best fit between theory and experiment since the experimental situation will always deviate from the ideal case in some way. We assume that the laser beam's intensity distribution follows a Gaussian distribution. We define the average value of Ω_R for the whole beam by taking the weighted average of a Gaussian distribution in the interval [0,FWHM/2], where FWHM is the full width at half maximum. Thus it follows that the Rabi frequency at the peak of the intensity distribution (see Fig. 1) is $\Omega_R = 0.721\Omega_{\text{peak}}$. From there the Rabi frequency of each region can be obtained by scaling by the value of the Gaussian distribution function.

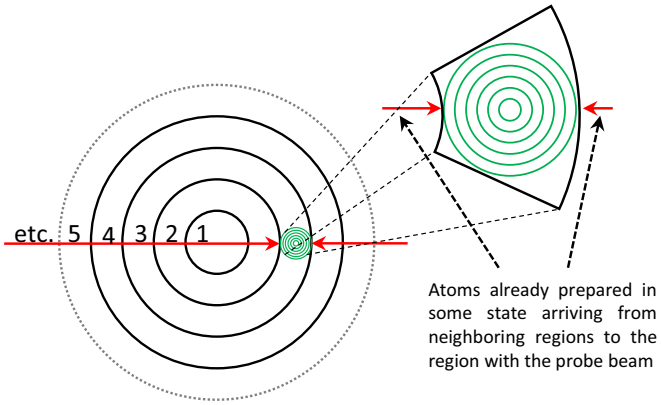

FIG. 2. Illustration of the way the theoretical calculations treat the pump beam (wide concentric rings) and the probe beam (a set of smaller rings in the third region of the pump beam). The atoms entering the region that contains the probe beam, have crossed multiple pump beam regions, thus they are already prepared in some state.

When modeling two beams (as in Sec. V), the multiregion approach is applied to each beam in the manner shown in Fig. 2. The wide beam is referred to as the pump beam, whereas the narrow beam is referred to as the probe beam. In this case, pump and probe refer to the beam diameter, which is related to their function in the experiment, rather than to the beam intensity. The reason is that the probe beam's function is to explore the population distribution of atoms inside the wider pump beam. It should be noted that the probe intensity in the outer regions of the pump beam can significantly exceed the pump beam intensity. Additionally the probe beam is always considered to be located inside one of the pump beam regions, and the width of the probe beam roughly coincides with the width of the pump beam region (see Fig. 2).

At first, Eq. (3) is used to calculate the density matrix that results from the interaction of the pump beam (divided into 20 regions) with the atoms while the probe beam is ignored. In the next step, the probe beam is divided into six regions out to 3 standard deviations (assuming a Gaussian probe beam). The pump intensity is taken to be constant over the probe beam, which means that the density matrix from the neighboring pump regions can be used to describe the atoms entering the probe beam from either side. The Hamiltonian and relaxation terms in Eq. (3) are now supplemented to include interactions with both probe and pump beam, and the system is solved for the regions of the probe beam in the presence of a pump field of constant intensity. For that purpose the index n in (3) is replaced with (n,m), and, following the same inference, one obtains equations for the description of two laser fields.

In the theoretical calculations the only observation direction is along the quantization axis.

III. EXPERIMENTAL SETUP

The theoretical model is tested with two experiments. The first experiment measures magneto-optical resonances on the D_1 line of ^{87}Rb and is shown schematically in Fig. 3. The experiment has been described elsewhere along with a

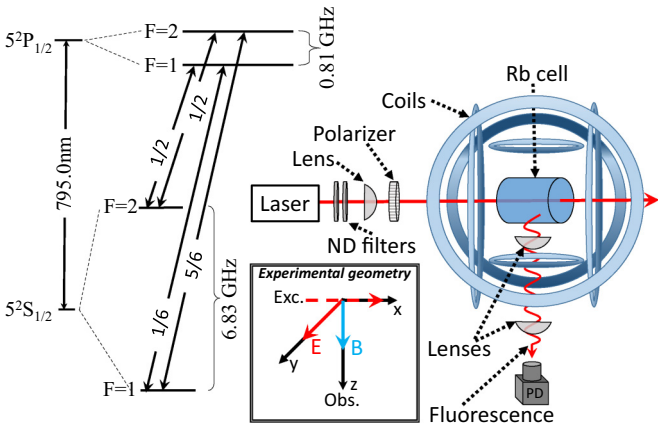

FIG. 3. Basic experimental setup for measuring magneto-optical resonances. The inset on the left shows the level diagram of ^{87}Rb [33]. The other inset shows the geometrical orientation of the electric field vector E, the magnetic field vector B, and laser propagation direction (Exc.) and observation direction (Obs.).

comparison to an earlier version of the theoretical model that did not divide the laser beam into separate regions [32].

The laser used in the experiment is an extended cavity diode laser, whose frequency can be scanned by applying a voltage to a piezo crystal attached to the grating. Neutral density (ND) filters are used to regulate the laser intensity, and linear polarization is obtained using a Glan-Thomson polarizer. A set of three orthogonal Helmholtz coils scans the magnetic field along the z axis while compensating the ambient field in the other directions. The Helmholtz coils also provide a homogeneous magnetic field inside the cell. The innermost coil has a diameter of 187.5 mm and consists of 225 turns of 1.5-mm diameter copper wire. A pyrex cell with a natural isotopic mixture of rubidium at room temperature is located at the center of the coils. The total laser-induced fluorescence (LIF) in a selected direction (without frequency or polarization selection) is detected with a photodiode (Thorlabs FDS-100 with active area of 13 mm^2) and data are acquired with a data acquisition card (National Instruments 6024E, analog-to-digital (AD) converter resolution, 12 bit; data rate, 50 kS/s) or a digital oscilloscope (Agilent DSO5014, AD converter resolution, 8 bit; data rate, 2.5 kS/s). To generate the magnetic field scan with a rate of about 1 Hz, a computer-controlled analog signal is applied to a bipolar power supply (Kepco BOP-50-8M). In the measurements currents up to 1 A are used, and the current stability was estimated to be around 0.5% of the rating. The laser frequency is simultaneously scanned at a rate of about 10–20 MHz/s, and is measured by a wave meter (HighFinesse WS-7). The laser beam is characterized using a beam profiler (Thorlabs BP104-VIS).

A second experimental setup is used to study the spatial profile of the fluorescence generated by atoms in a laser beam at resonance. It is shown in Fig. 4. Here two lasers are used to excite the D_1 and D_2 transitions of cesium. Both lasers are based on distributed feedback diodes from Toptica (DL100-DFB, both tunable in 25-GHz frequency range). One of the lasers (Cs D_2) serves as a pump laser with a spatially broad and intense beam, while the other (Cs D_1), spatially narrower beam probes the fluorescence dynamics within the pump beam. Figure 5 shows the level scheme of the excited transitions. Both lasers are stabilized with saturation absorption signals from cells shielded by three layers of mu-metal. Mu-metal shields are used to avoid frequency drifts due to the magnetic field scan performed in the experiment and other magnetic field fluctuations in the laboratory.

To reduce the amount of scattered light entering the detector, the cesium cell is wrapped in black paper with a small opening (5 mm $\times$2 mm) for fluorescence measurements. A bandpass filter (890 nm $\pm$ 10 nm) is placed before the photodiode. To reduce noise from the intense pump beam, the probe beam is modulated by placing a mechanical chopper (providing a 2.4-kHz chopping frequency) near its focus, and

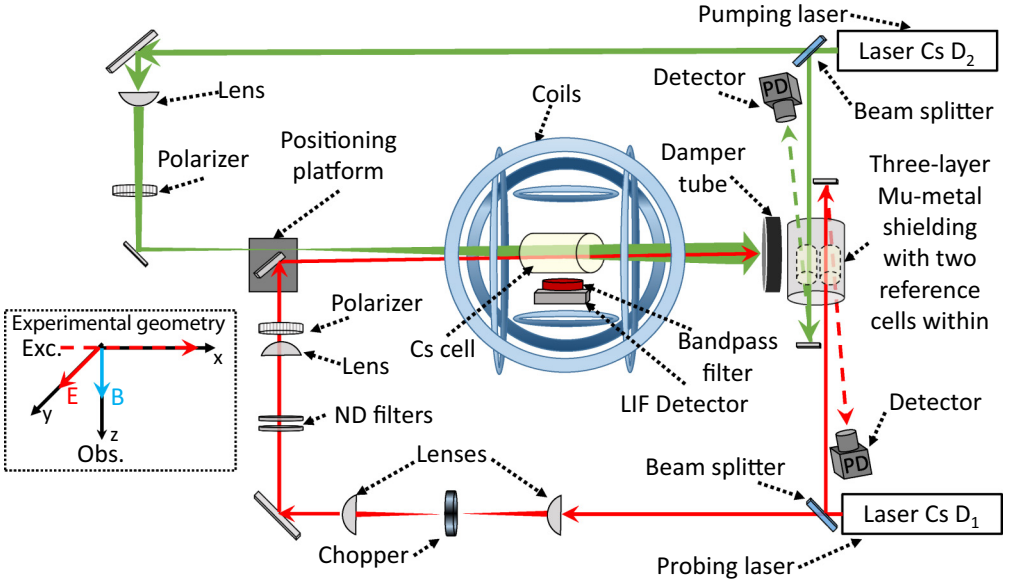

FIG. 4. Experimental setup for the two-laser experiment. The lasers are stabilized by two Toptica Digilok modules locked to error signals generated from saturated absorption spectroscopy measurements made in separate, magnetically shielded cells.

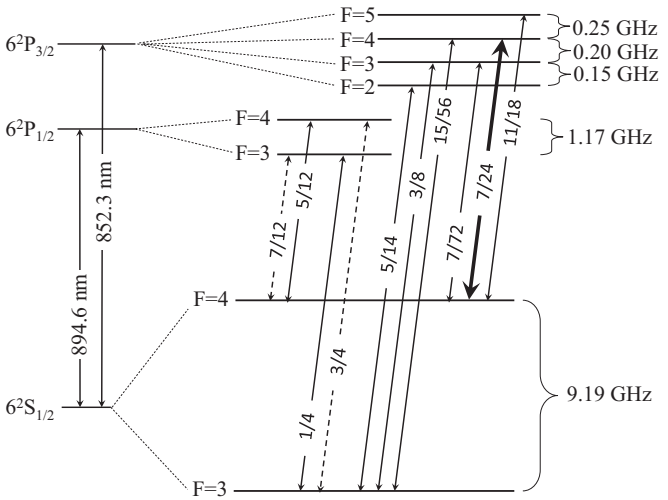

FIG. 5. Level scheme for the two-laser experiment. The bold, solid arrow represents the pump laser transition, whereas the arrows with dashed lines represent the scanning laser transitions. Other transitions are given as thin, solid lines.

the fluorescence signal passes through a lock-in amplifier and is recorded on a digital oscilloscope (Yokogawa DL-6154, AD converter resolution, 8 bit; data rate, 2.5 kS/s). The probe laser is scanned through the pump laser beam profile using a mirror mounted on a moving platform (Nanomax MAX301 from Thorlabs) with a scan range of 8 mm in one dimension. The probing beam itself has a FWHM diameter of 200 μm with typical laser power of 100 μW. The pump beam width is 1.3 mm (FWHM), and its power is 40 mW. This laser beam diameter is achieved by letting the laser beam slowly diverge after passing the focal point of a lens with focal length of 1 m. The pump laser beam diverges slowly enough so that the beam diameter within the vapor cell is effectively constant. The probe beam is also focused by an identical lens to reach its focus point inside the cell.

In both experiments described in this section, the estimated solid angle of fluorescence observation is around 0.02 sr.

IV. APPLICATION OF THE MODEL TO MAGNETO-OPTICAL SIGNALS OBTAINED FOR HIGH LASER POWER DENSITIES

As a first test of the numerical model with multiple regions inside the laser beam, we use the model to calculate the shapes of magneto-optical resonances for ^{87}Rb in an optical cell. The experimental setup has been described earlier (see Fig. 3). Figures 6(a)–6(c) show experimental signals (dots) and theoretical calculations (curves) of magneto-optical signals in the $F_g = 2 \longrightarrow F_e = 1$ transition of the D_1 line of ^{87}Rb. Three theoretical curves are shown: Curve N1 is calculated assuming a laser beam with a single average intensity; curve N20 is calculated using a laser beam divided into 20 concentric regions of equal width, and assuming that all the particles traverse the laser beam crossing its center; curve N20MT is calculated in the same way as curve N20, but furthermore the results are averaged also over trajectories that did not pass through the center, i.e., taking into account the particles that

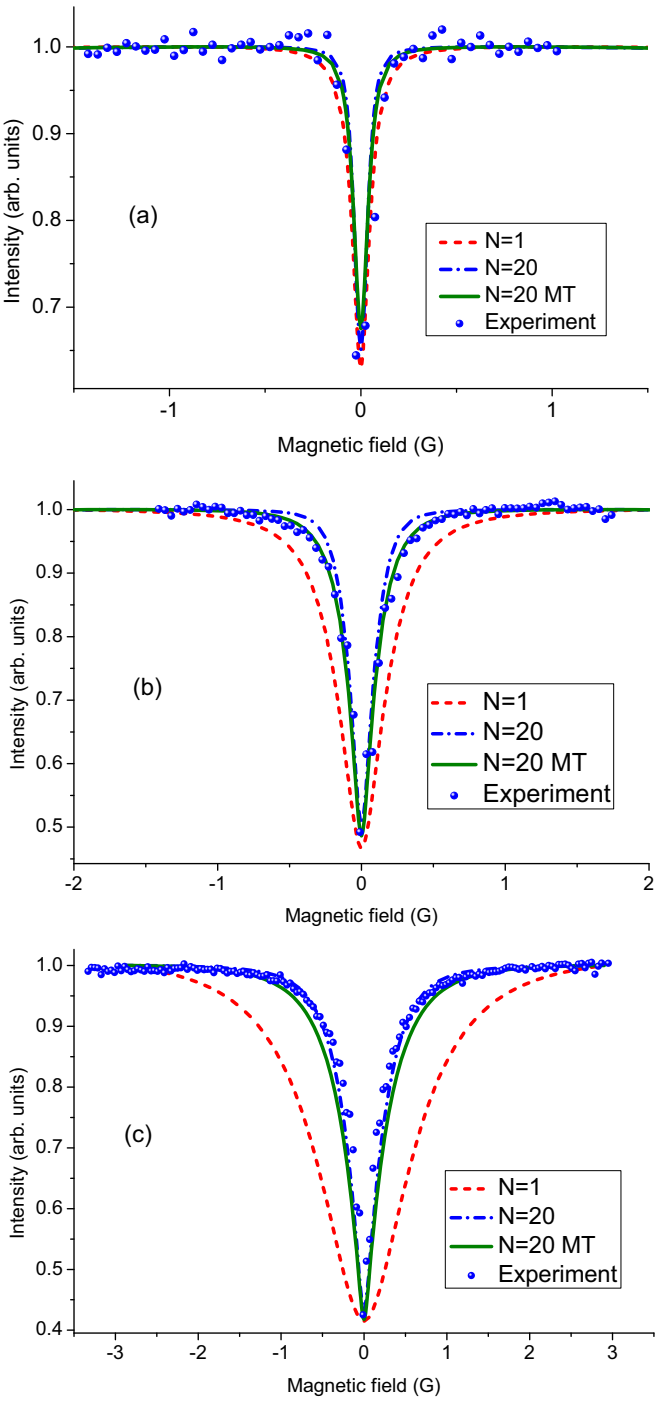

FIG. 6. Magneto-optical resonances for the $F_g = 2 \longrightarrow F_e = 1$ transition of the D_1 line of ^{87}Rb. Solid circles represent experimental measurements for (a) 28 μW (Ω_R=2.5 MHz), (b) 280 μW (Ω_R=8.0 MHz), and (c) 2800 μW (Ω_R=25 MHz). Curve N1 (dashed) shows the results of a theoretical model that uses one Rabi frequency to model the entire beam profile. Curve N20 (dash-dotted) shows the result of the calculation when the laser beam profile is divided into 20 concentric rings, and the optical Bloch equations are solved separately for each ring. Curve N20MT (solid) shows the results for a calculation with 20 concentric regions when trajectories are taken into account that do not pass through the center of the beam.

skim the Gaussian laser beam profile wings. As the model starts to converge rapidly with only 10 regions and with diminishing returns for using additional regions, we choose 20 regions because the computational cost is reasonable and the accuracy is more than sufficient even at the highest laser power densities. At the relatively low Rabi frequency of $\Omega_R = 2.5$ MHz [Fig. 6(a)] all calculated curves practically coincide and describe well the experimental signals. The single region model treats the beam as a cylindrical beam with an intensity of 2 mW/cm^2, which is below the saturation intensity for that transition of 4.5 mW/cm^2 [33]. When the laser intensity is 20 mW/cm^2 ($\Omega_R = 8.0$ MHz), well above the saturation intensity, model N1 is no longer adequate for describing the experimental signals and model N20MT works slightly better [Fig. 6(b)]. In particular, the resonance becomes sharper and sharper as the intensity increases, and models N20 and N20MT reproduce this sharpness. Even at an intensity around 200 mW/cm^2 ($\Omega_R = 25$ MHz), the models with 20 regions describe the shape of the experimental curve quite well, while model N1 describes the experimental results poorly in terms of width and overall shape [Fig. 6(c)].

V. INVESTIGATION OF THE SPATIAL DISTRIBUTION OF FLUORESCENCE IN AN INTENSE LASER BEAM

A. Theoretical investigation of the spatial dynamics of fluorescence in an extended beam

In order to describe the magneto-optical signals in the previous sections, the fluorescence from all concentric beam regions in models N20 and N20MT is summed, since usually experiments measure only total fluorescence (or absorption), especially if the beams are narrow. However, solving the optical Bloch equations separately for different concentric regions of the laser beam, it is possible to calculate the strength of the fluorescence as a function of distance from the center of the beam. With an appropriate experimental technique, the distribution of fluorescence within a laser beam can also be measured.

Figure 7 shows the calculated fluorescence distribution as a function of position in the laser beam. As atoms move through the beam in one direction, the intense laser radiation optically pumps the ground state. In a very intense beam, the ground-state levels that can absorb light have been emptied while traversing the outer regions, and thus the fluorescence intensity of the central regions will decrease (solid, green curve). Since atoms are actually traversing the beam from all directions, the result is a fluorescence profile with a reduced intensity in the central regions of the beam (dashed, red curve).

The effect of increasing the laser beam intensity (or Rabi frequency) can be seen in Fig. 8. At a Rabi frequency of $\Omega_R = 0.6$ MHz, the fluorescence profile tracks the intensity profile of the laser beam exactly. When the Rabi frequency is increased 10 times ($\Omega_R = 6.0$ MHz), which corresponds to an intensity increase of 100, the fluorescence profile already appears somewhat deformed and wider than the actual laser beam profile. At Rabi frequencies of $\Omega_R = 48.0$ MHz and greater, the fluorescence intensity at the center of the intense laser beam is weaker than towards the edges as a result of the ground state being depleted by the intense radiation before the

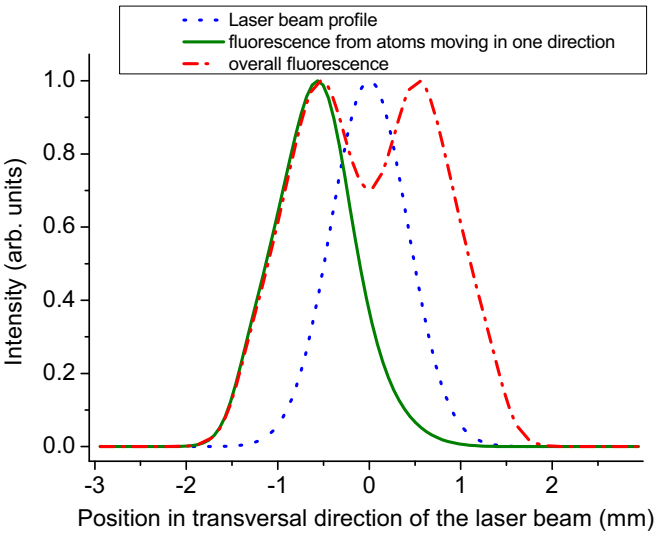

FIG. 7. Theoretical simulation of fluorescence distribution in an intense laser beam, where zero marks the center of the laser beam. Dotted (blue) line—laser beam profile, solid (green) line—fluorescence from atoms moving in one direction; dash-dotted (red) line—the overall fluorescence as a function of position that results from averaging all beam trajectories.

atoms reach the center of the laser beam. If one were to excite a dark state using an intense beam with a much larger radius, the resulting fluorescence distribution would be expected to look like an intense (narrow) ring at the border of the laser beam, and the inner regions would exhibit a flat, less intense structure. If one were to excite a bright state with such a beam, one would expect a roughly Gaussian fluorescence distribution with a flattened top.

B. Experimental study of the spatial dynamics of excitation and fluorescence in an intense, extended beam

In order to test our theoretical model of the spatial distribution of fluorescence from atoms in an intense, extended pumping beam, we record magneto-optical resonances from

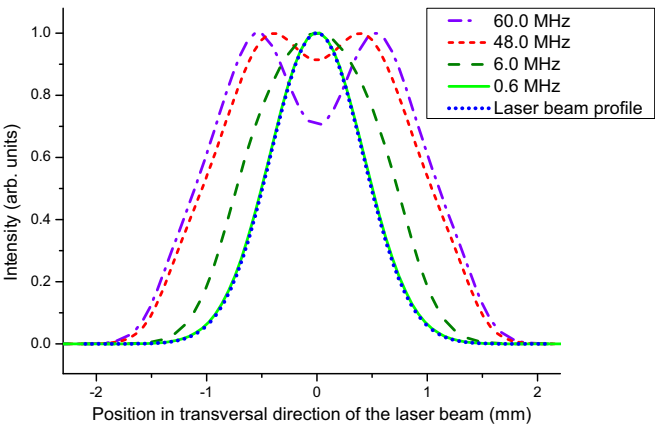

FIG. 8. Calculated fluorescence distribution as a function of position in the laser beam for various values of the Rabi frequency. As the Rabi frequency increases, the distribution becomes broader.

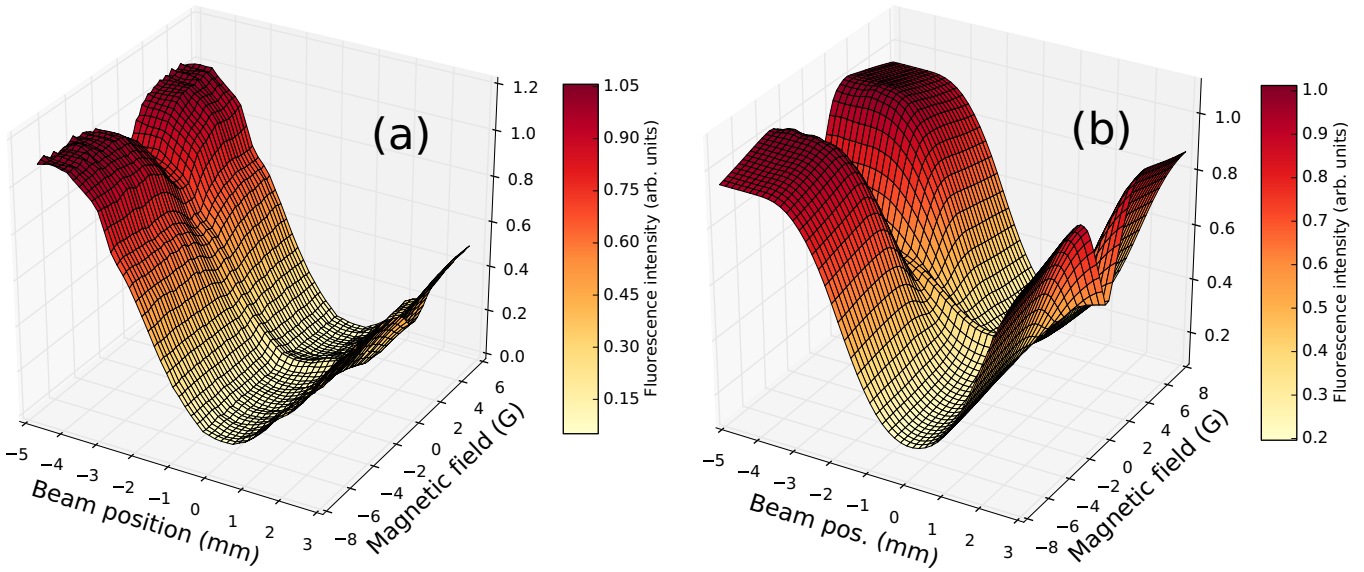

FIG. 9. Magneto-optical resonances produced for various positions of the probing laser beam ($F_g = 4 \longrightarrow F_e = 3$ transition of the D_1 line of cesium) with respect to the pump laser beam ($F_g = 4 \longrightarrow F_e = 4$ transition of the D_2 line of cesium). (a) Experimental results and (b) theoretical calculations.

various positions in the pumping beam. As the probe beam used in this experiment is relatively strong, the multiple region approach is also applied to it, and in the calculations the probe beam is divided into six regions (see Fig. 2 and the accompanying description in Sec. II for details on the treatment of two beams). It has to be pointed out that the experiment with the two laser beams is performed in order to cross-check the theoretical model with the multiple region approach, and the coincidence between calculations and the experiment is expected to be qualitative. Thus, there are some approximations done to make the calculation times reasonable. In particular, by two stages of the calculations described in Sec. II, we assume that the probe beam does not contribute to the preparation of atoms that fly into the region with the two beams (pump and probe). Besides that, only trajectories crossing the center of the pump beam are taken into account, and the width of the probe beam is considered to coincide with the width of a pump beam region.

The experimental setup is shown in Fig. 4. To visualize these data, surface plots are generated where one horizontal axis represents the magnetic field and the other, the position of the probe beam relative to the pump beam axis. The height of the surface represents the fluorescence intensity. In essence, the surface consists of a series of magneto-optical resonances

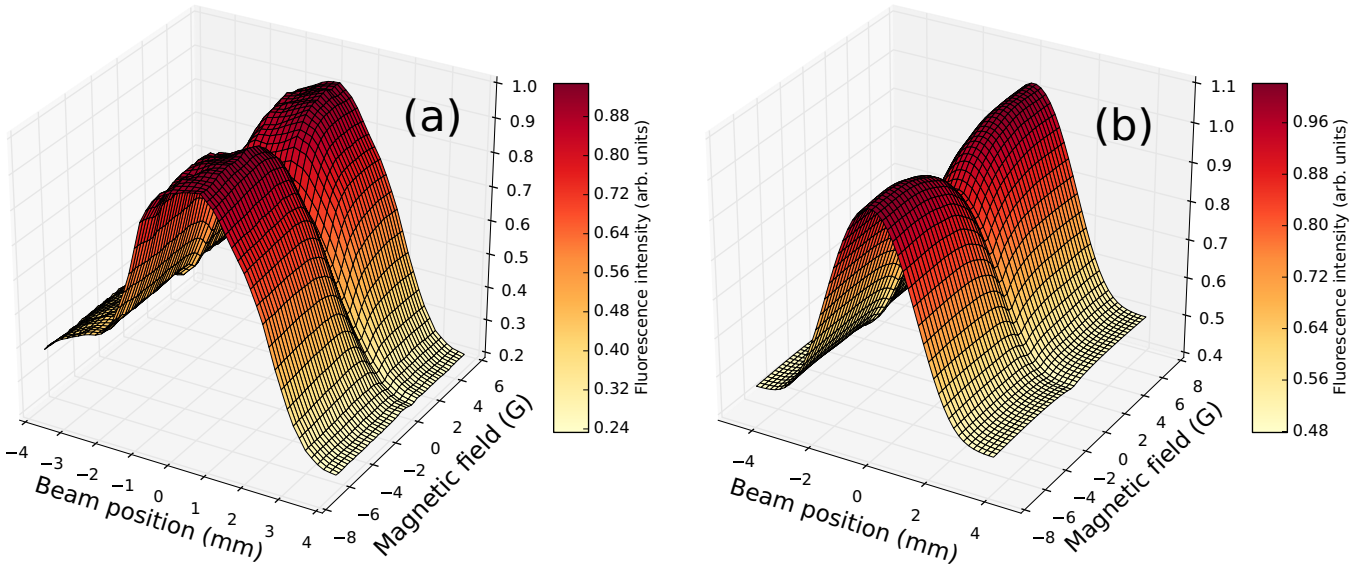

FIG. 10. Magneto-optical resonances produced for various positions of the probe laser beam ($F_g = 3 \longrightarrow F_e = 4$ transition of the D_1 line of cesium) with respect to the pump laser beam ($F_g = 4 \longrightarrow F_e = 4$ transition of the D_2 line of cesium). (a) Experimental results and (b) theoretical calculations.

recorded for a series of positions of the probe beam axis relative to the pump beam axis. Figure 9 shows the results for experiments [Fig. 9(a)] and calculations [Fig. 9(b)] for the pump beam tuned to the $F_g = 4 \longrightarrow F_e = 4$ transition of the Cs D_2 line and the probe beam tuned to the $F_g = 4 \longrightarrow F_e = 3$ transition of the Cs D_1 line.

One can see that the theoretical plot reproduces qualitatively all the features of the experimental measurement. Similar agreement can be observed when the probe beam is tuned to the $F_g = 3 \longrightarrow F_e = 4$ transition of the Cs D_1 line, as shown in Fig. 10.

VI. CONCLUSIONS

We show how to model magneto-optical signals more accurately at laser intensities significantly higher than the saturation intensity by dividing the laser beam into concentric circular regions and solving the rate equations for Zeeman coherences in each region while taking into account the actual laser intensity in that region and the transport of atoms between regions. We discuss results of using this approach for modeling magneto-optical resonances for the $F_g = 2 \longrightarrow F_e = 1$ transitions of the D_1 line of ^{87}Rb, comparing the calculated curves to measured signals. We demonstrate that good agreement between theory and experiment can be achieved up to Rabi frequencies of at least 25 MHz, which corresponds to a laser intensity of 200 mW/cm^2, or more than 40 times the saturation intensity of the transition. As an additional check on the model, we present results from a theoretical and experimental study of the spatial distribution of the fluorescence intensity within a laser beam. The results indicate that at high laser power densities, the maximum fluorescence intensity is not produced in the center of the beam, because the atoms have been pumped free of absorbing levels prior to reaching the center. We compare experimental and theoretical signals of magneto-optical resonance signals obtained by exciting cesium atoms with a narrow probe beam tuned to the D_1 transition at various locations inside a region illuminated by an intense pump beam tuned to the D_2 transition and obtain good qualitative agreement.

ACKNOWLEDGMENTS

We gratefully acknowledge support from Latvian Science Council Grant No. 119/2012, and from University of Latvia Academic Development Project No. AAP2015/B013.

[1] S. E. Harris, J. E. Field, and A. Imamoglu, Phys. Rev. Lett. **64**, 1107 (1990).
[2] L. V. Hau, S. E. Harris, Z. Dutton, and C. H. Behroozi, Nature (London) **397**, 594 (1999).
[3] C. Liu, Z. Dutton, C. H. Behroozi, and L. V. Hau, Nature (London) **409**, 490 (2001).
[4] M. O. Scully and M. Fleischhauer, Phys. Rev. Lett. **69**, 1360 (1992).
[5] D. Budker and M. V. Romalis, Nature Physics **3**, 227 (2007).
[6] S. Knappe, P. D. D. Schwindt, V. Shah, L. Hollberg, J. Kitching, L. Liew, and J. Moreland, Opt. Express **13**, 1249 (2005).
[7] D. Budker, W. Gawlik, D. F. Kimball, S. M. Rochester, V. V. Yashchuk, and A. Weis, Rev. Mod. Phys. **74**, 1153 (2002).
[8] B. C. Regan, E. D. Commins, C. J. Schmidt, and D. DeMille, Phys. Rev. Lett. **88**, 071805 (2002).
[9] M. Auzinsh, D. Budker, and S. M. Rochester, *Optically Polarized Atoms* (Oxford University Press, Oxford, 2010).
[10] E. Arimondo, in *Elsevier Science B.V.*, Vol. 35 (Elsevier, Amsterdam, 1996), p. 259.
[11] J. C. Lehmann and C. Cohen-Tannoudji, C. R. Acad. Sci. (Paris) **258**, 4463 (1964).
[12] E. B. Alexandrov, M. Auzinsh, D. Budker, D. F. Kimball, S. Rochester, and V. V. Yashchuk, J. Opt. Soc. Am. B **22**, 7 (2005).
[13] A. P. Kazantsev, V. S. Smirnov, A. M. Tumaikin, and I. A. Yagofarov, Opt. Spectrosk. (USSR) **57**, 116 (1984).
[14] F. Renzoni, S. Cartaleva, G. Alzetta, and E. Arimondo, Phys. Rev. A **63**, 065401 (2001).
[15] J. Alnis and M. Auzinsh, Phys. Rev. A **63**, 023407 (2001).
[16] J. L. Picqué, J. Phys. B **11**, L59 (1978).
[17] M. Auzinsh, R. Ferber, F. Gahbauer, A. Jarmola, and L. Kalvans, Phys. Rev. A **78**, 013417 (2008).
[18] N. Castagna and A. Weis, Phys. Rev. A **84**, 053421 (2011).
[19] E. Breschi and A. Weis, Phys. Rev. A **86**, 053427 (2012).
[20] M. P. Auzinsh, R. S. Ferber, and I. Y. Pirags, J. Phys. B **16**, 2759 (1983).
[21] C. Andreeva, S. Cartaleva, L. Petrov, S. M. Saltiel, D. Sarkisyan, T. Varzhapetyan, D. Bloch, and M. Ducloy, Phys. Rev. A **76**, 013837 (2007).
[22] G. Alzetta, S. Gozzini, A. Lucchesini, S. Cartaleva, T. Karaulanov, C. Marinelli, and L. Moi, Phys. Rev. A **69**, 063815 (2004).
[23] M. Auzinsh, A. Berzins, R. Ferber, F. Gahbauer, L. Kalvans, A. Mozers, and D. Opalevs, Phys. Rev. A **85**, 033418 (2012).
[24] M. Auzinsh, A. Berzins, R. Ferber, F. Gahbauer, U. Kalnins, L. Kalvans, R. Rundans, and D. Sarkisyan, Phys. Rev. A **91**, 023410 (2015).
[25] K. Blushs and M. Auzinsh, Phys. Rev. A **69**, 063806 (2004).
[26] M. Auzinsh, A. Berzins, R. Ferber, F. Gahbauer, L. Kalvans, A. Mozers, and A. Spiss, Phys. Rev. A **87**, 033412 (2013).
[27] L. Allen and J. H. Eberly, *Optical Resonance and Two Level Atoms* (Wiley, New York, 1975).
[28] N. G. van Kampen, Phys. Rep. **24**, 171 (1976).
[29] M. Auzinsh and R. Ferber, *Optical Polarization of Molecules* (Cambridge University Press, Cambridge, 2005).
[30] J. P. Barrat and C. Cohen-Tannoudji, J. Phys. Radium **22**, 443 (1961).
[31] M. I. Dyakonov, Sov. Phys. JETP **20**, 6 (1965).
[32] M. Auzinsh, R. Ferber, F. Gahbauer, A. Jarmola, and L. Kalvans, Phys. Rev. A **79**, 053404 (2009).
[33] D. A. Steck, *Rubidium 87 D Line Data*, Revision 2.1.2 (University of Oregon, Eugene, 2009).